Nanotechnology

PAPER

Improved optical imaging of high aspect ratio nanostructures using dark-field microscopy

IOP Publishing Nanotechnology
Nanotechnology 30 (2019) 285301 (8pp) https://doi.org/10.1088/1361-6528/ab13de

Improved optical imaging of high aspect ratio nanostructures using dark-field microscopy

R R A Syms, O Sydoruk and A Bouchaala

Optical and Semiconductor Devices Group, EEE Dept., Imperial College London, Exhibition Road, London SW7 2AZ, United Kingdom

E-mail: r.syms@imperial.ac.uk

Received 29 December 2018, revised 22 February 2019
Accepted for publication 27 March 2019
Published 24 April 2019

Abstract

Improvements to white light optical imaging of widely spaced, high aspect ratio nanostructures are demonstrated using dark-field field microscopy. 1D models of bright- and dark-field imaging are developed from rigorous modal diffraction theory by assuming that features are periodic. A simple model is developed to explain dark field results and simulated line images obtained using the two modalities are compared for different dimensions and materials. Increased contrast between etched features and the substrate is demonstrated in dark field, due to its reduced sensitivity to scattering from flat areas. The results are verified using silicon nanostructures fabricated by sidewall transfer lithography, and feature separation with improved tolerance to apparent substrate brightness is demonstrated during image segmentation using the Otsu method.

Keywords: NEMS, MEMS, sub-wavelength imaging, image segmentation

1. Introduction

The need for high-aspect ratio (HAR) nanoscale features in ultrasensitive silicon nanoelectromechanical systems (NEMS) [1, 2] is posing new difficulties. Low-cost fabrication and inspection methods are needed to avoid time-consuming electron-beam writing and scanning electron microscope inspection. Processes such as sidewall transfer lithography (STL) allow parallel fabrication of restricted feature sets. This method combines repeated STL (originally developed for field-effect transistor fabrication [3, 4] and subsequently used for other features such as nanowires [5]) with standard MEMS processing [6, 7] to form more general structures [8, 9]. However, the need for metrology remains.

The visibility of widely spaced sub-micron features in an optical microscope [10] suggests an obvious approach. We have previously shown that HAR NEMS are visible in bright field with white light illumination [11]. Nanostructures cannot be properly resolved, but appear as wider dark lines; microstructures appear as dark lines at feature edges. We have also used local curvature of the brightness surface [12, 13] to extract both types of feature, allowing separate reconstruction of NEMS and MEMS parts. However, because of background variations, features are still insufficiently differentiated for reliable separation using standard image segmentation techniques such as the Otsu method [14, 15].

Here, we show that dark-field illumination provides more suitable starting images, through its reduced sensitivity to scattering from flat surfaces. In section 2, we extend work by Hopkins [16], Nyssonen [17, 18] and Sheridan [19–21] on imaging of periodic features to develop models of white-light imaging in both modalities. We use rigorous modal diffraction theory [22–26] to predict line images, show that dark-field provides inherently greater contrast between etched features and the substrate, and provide an approximate analytic explanation. In section 3, we verify the predictions experimentally using silicon NEMS, and show that feature extraction with improved tolerance to substrate variations is obtained in dark field. Conclusions are drawn in section 4.

2. Theoretical model

Models of bright- and dark-field imaging are shown in figures 1(a) and (b), respectively, the first being previously described in [11]. The surface for imaging is modeled as a

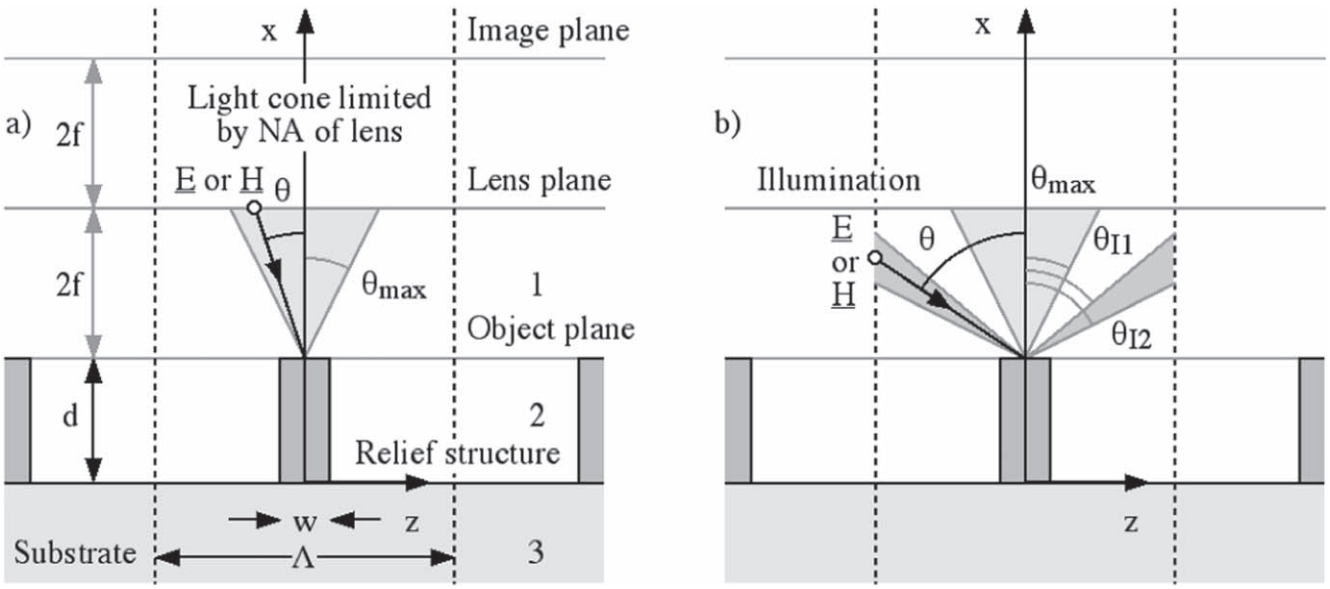

Figure 1. Theoretical models of (a) bright- and (b) dark-field imaging.

relief structure of period Λ, consisting of a semi-infinite substrate of relative dielectric constant ε_{r3} (Layer 3) carrying a set of vertical ribs of width w and depth d formed in a material with $\varepsilon_r = \varepsilon_{r2a}$ surrounded by air (ε_{r2b}) (Layer 2) and capped by further semi-infinite layer of air (Layer 1; $\varepsilon_{r1} = \varepsilon_{r2b}$).

Kohler illumination is modeled using a coherent summation of the effects of plane waves incident at a discrete set of angles, and white light imaging by an incoherent sum of similar effects at a discrete set of wavelengths. Differences between the imaging modalities lie only in the range of incidence angles. In bright field, illumination is carried out using a light cone matching that used for light collection. Assuming a lens of a given numerical aperture (NA), the angular range is from $-\theta_{max}$ to θ_{max}, where $\theta_{max} = \sin^{-1}$(NA) In dark field, a hollow light cone is used, lying outside the light collection cone and ranging from $\pm\theta_{I1}$ to $\pm\theta_{I2}$ with $\theta_{I1} > \theta_{max}$. Backscattered light is collected using the lens and used to form a line image with unity magnification. In general, the backscatter will consist of propagating and evanescent diffraction orders; however, only propagating orders lying within an angular range $\pm\theta_{max}$ can contribute to the image.

Numerical methods may be used to find the backscattered field for a single incidence angle, wavelength and polarization. However, only semi-analytic approaches such as the modal method [22–24] are currently fast enough for such calculations to be practical for multiple incident waves. Full details have been given many times elsewhere. Here, we merely state that the permittivity distribution in layer 2 is first expanded as a Fourier series. Field solutions are then assumed in terms of the incident wave and a set of reflected diffraction orders in Layer 1, a set of eigenmodes formed from a sum of counter-propagating terms in Layer 2, and a set of transmitted diffraction orders in Layer 3. The Floquet theorem is then used to find the k-vectors of the diffraction orders and the constituents of the eigenmodes. Finally, matching of tangential electric and magnetic fields at the boundaries between Layers 1 and 2 and Layers 2 and 3 is used to construct simultaneous equations that may be solved to find the amplitudes of all diffraction orders and eigenmodes. The procedure is straightforward, but accurate results involve lengthy calculations.

Here, the substrate and relief structure are assumed formed in silicon (whose relative dielectric constant is taken constant for simplicity, as $\varepsilon_{r3} = \varepsilon_{r2a} = 11.7$—j0.272), surrounded by air ($\varepsilon_{r2b} = \varepsilon_{r1} = 1$). Features are initially assumed etched to a constant depth $d = 4\ \mu$m, with a period $\Lambda = 10\ \mu$m and a variable width w. Three lenses are modeled, having acceptance cones with $\theta_{max} = 10°$, 20° and 30°, respectively. For dark-field, the illumination cone is taken to have bounding angles $\theta_{I1} = \theta_{max} + 5°$, $\theta_{I2} = \theta_{I1} + 10°$. In each modality, white light illumination is modeled by summing the effects of 21 angles of incidence over the allowed angular range and 21 wavelengths between 400 and 700 nm. Illuminating and backscattered waves are weighted by aplanatic factors, and only diffraction orders lying within the acceptance cone contribute to the image.

Similar results are obtained for TE or TM polarization; here we show only TE. Figure 2 shows simulated line images of nanostructures with $w = 0.1\ \mu$m (black lines) and microstructures with $w = 2\ \mu$m (gray lines), obtained using (a) bright-and (b) dark-field imaging, which highlight differences between the modalities. In each case, the image brightness has been normalized to the maximum obtained for the nanoscale feature. In bright field, the image brightness of a uniform substrate should be constant. Here (figure 2(a)), it is high except near the nanostructure, where it reduces by around 60%. However, the apparent half-width is much greater than the actual feature size. The effect of increasing NA is to reduce the half-width, without significantly affecting the brightness modulation. There are shallower troughs in brightness at the edges of the microstructure. The effect of

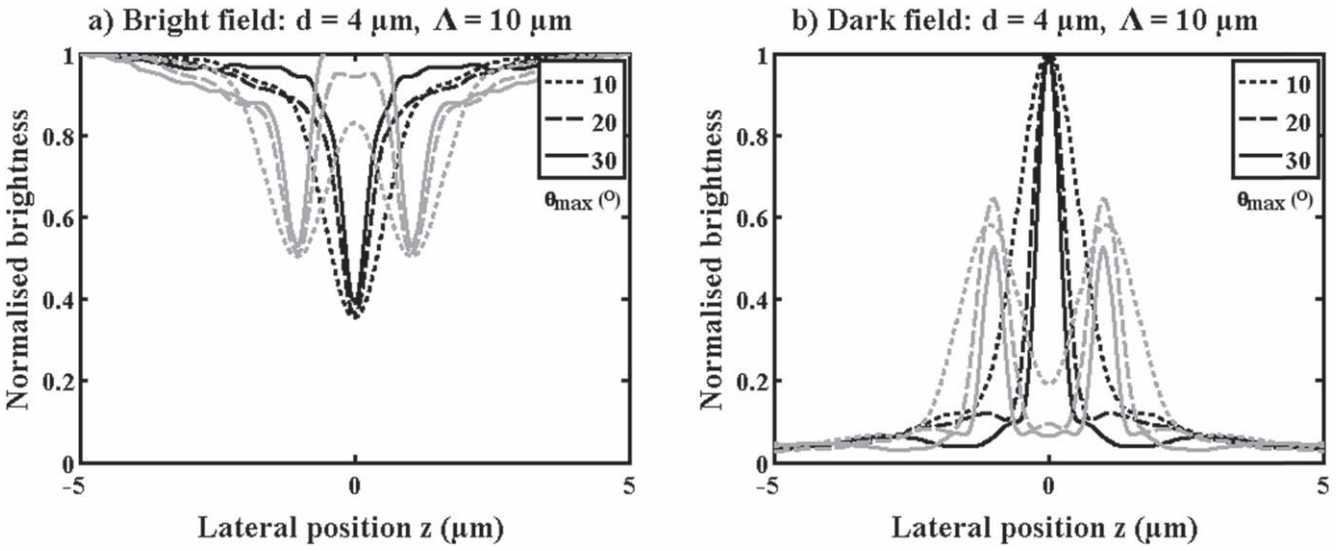

Figure 2. Simulated line images of nanoscale ($w = 0.1\ \mu$m; black) and microscale ($w = 2.0\ \mu$m; gray) features, obtained using (a) bright- and (b) dark-field illumination. In each case, $d = 4\ \mu$m, $\Lambda = 10\ \mu$m, and results are shown for lenses with different θ_{max}.

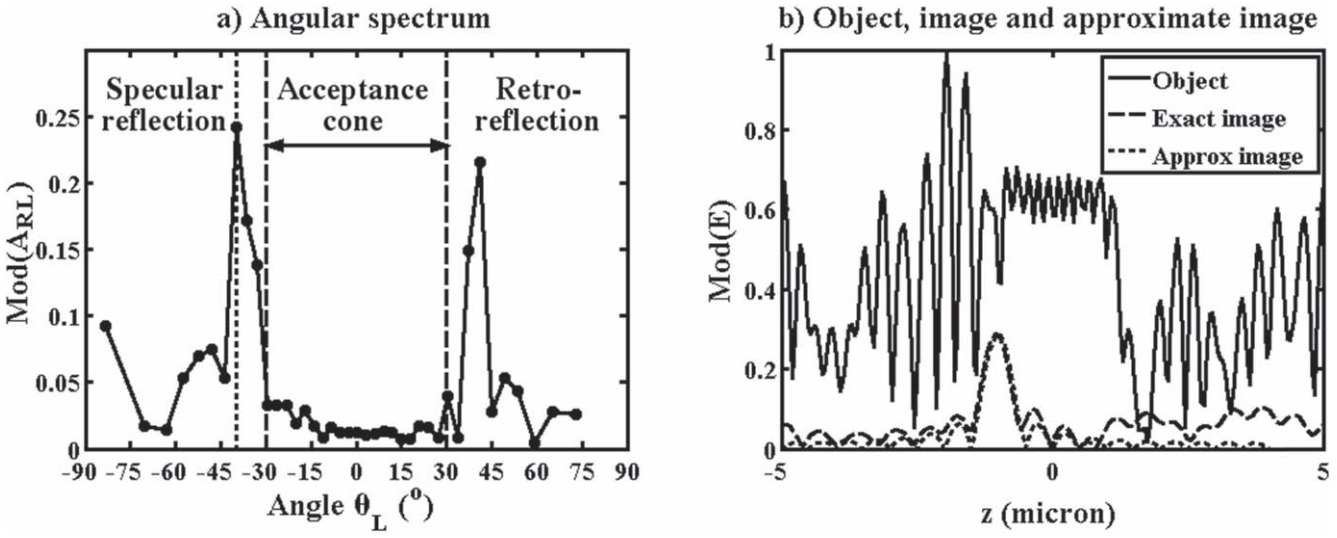

Figure 3. (a) Angular spectrum of diffraction orders and (b) object, image and approximate image of microscale feature obtained in dark field illumination, calculated assuming $w = 2\ \mu$m, $d = 4\ \mu$m, $\Lambda = 10\ \mu$m, $\theta = 40^\circ$ and $\theta_{max} = 30^\circ$.

increasing NA is again to improve the sharpness and separation of the troughs, without significantly affecting their depth.

In dark-field illumination, a flat substrate should appear completely dark. Here (figure 2(b)), the image brightness is low except near the nanostructure, where it increases considerably. On this basis, dark field illumination yields greater contrast between nanoscale features and the substrate. Similarly, there are peaks in brightness at the edges of the microstructure. However, for each lens, the peak remains at about half the value obtained with a nanostructure. Thus, dark field also yields greater contrast between nanoscale and microscale features.

A qualitative explanation for dark-field results may be provided as follows. Figure 3(a) shows the angular spectrum of reflected orders obtained for Si mesas with $w = 2\ \mu$m, $d = 4\ \mu$m and $\Lambda = 10\ \mu$m, for a single wave incident at $\theta = 40^\circ$, $\lambda = 0.5\ \mu$m. The peaks at $\theta = -40^\circ$ and $\theta = +40^\circ$ correspond to specular reflection and retro-reflection, respectively. Within the acceptance angle $-30^\circ < \theta < +30^\circ$ of the lens with the highest NA considered, the amplitudes of the diffraction orders are both small and approximately constant. This result is consistent with the geometrical theory of diffraction, which predicts that scattering from a conducting wedge will take the form of a weak cylindrical wave [27, 28].

Assuming that the lens accepts diffraction orders in the range $L_1 < L < L_2$, and making the simplifying approximation that the amplitudes of any accepted orders are equal to A_0, the image field can be written as:

$$A(z) = A_0 \sum_{L1}^{L2} \exp\{-j(k_z + LK)z\}. \quad (1)$$

Here k_z is the z-component of the incident wave and $K = 2\pi/\Lambda$. Substituting $L = L_0 + \Delta L$, where $L_0 = (L_2 + L_1)/2$,

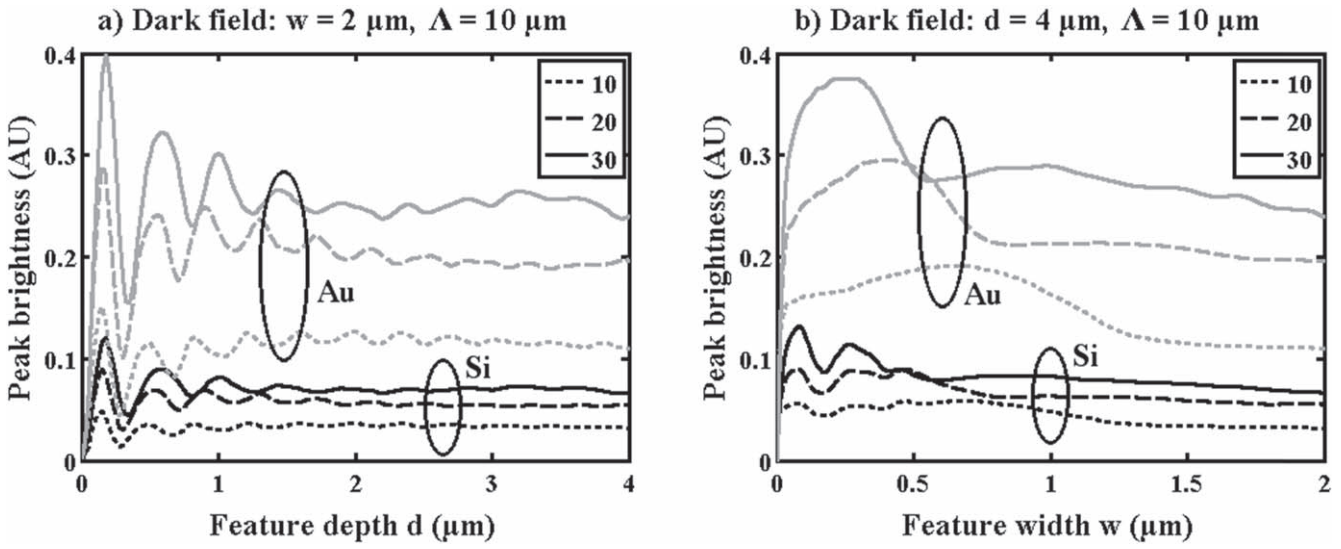

Figure 4. Variation of dark-field image maxima, (a) with depth, for $w = 2\ \mu$m, and (b) with width, for $d = 4\ \mu$m. In each case, $\Lambda = 10\ \mu$m, and results are shown in black for Si and gray for Au, for lenses with different θ_{max}.

we may obtain the modulus of the image as:

$$|A(z)| = A_0 \left| \sum_{-M}^{+M} \exp\{-j\Delta LKz\} \right|. \quad (2)$$

Here $M = (L_2 - L_1)/2$, and can be found approximately as $M = \theta_{max}\Lambda/\lambda$, or around 10 for the parameters of figure 3(a). Summation then gives:

$$\left\{ |A(z)| = A_0 \left| \frac{\sin\{NK(z + w/2)/2\}}{\sin(Kz/2)} \right| \right\}. \quad (3)$$

Here $N = 2M + 1$. Equation (3) predicts that the image will be a sinc-type function, and an assumed shift in position has been used to locate the peak at $z = -w/2$.

This expression appears remarkably accurate, despite its simplicity. Figure 3(b) compares the moduli of the 'object' field at $x = 0$ for the parameters in figure 3(a), the exact 'image' obtained by filtering the spectrum of diffraction orders, and the approximate image obtained from (3) using a matched value of A_0. The object field is dominated by interference between the reflected and retro-reflected waves, and is largely devoid of useful detail. However, the agreement between the exact and approximate image is excellent.

The implication is that the mesa will largely be visible through its leading edge, and that its appearance will follow from the square of the expression in (3). Illumination at the opposite angle will generate a similar response at $z = +w/2$. Wide structures will therefore be visible as two separate peaks in brightness, while sufficiently small structures will appear as a larger merged peak. Finally, any improvement in discrimination obtained in dark field must follow from the removal of reflected and retro-reflected waves from the image.

Although we have not performed an exhaustive parameter search, these characteristics appear consistent. For example, the black lines in figure 4(a) shows the variation of the dark field image maxima with feature depth, for Si microstructures with $w = 2\ \mu$m, in arbitrary units. Similar variations are obtained for all three lenses. The maxima rise rapidly at small d, and show oscillations consistent with coherent addition of reflections from the substrate and mesa surface. However, these reduce as d rises, when the addition becomes incoherent. The gray lines show results for structures formed in gold, here for simplicity taken as a having a frequency-independent permittivity $\varepsilon_{r3} = \varepsilon_{r2a} = -8.4953 - j1.6239$. Similar characteristic behavior is seen, but with larger overall peaks following from increased reflectivity and suggesting an alternative contrast mechanism in structures formed from mixed materials.

The black lines in figure 4(b) shows the variation of dark field maxima with feature width, for $d = 4\ \mu$m. The maxima again rise rapidly at small w to peaks at around $w = 0.1\ \mu$m before gradually reducing to approximately constant values when $w = 2\ \mu$m. Intermediate oscillations are, we believe, associated with excitation of in-plane resonances within vertical ribs. The gray lines show corresponding results for gold; there the resonant features are largely absent, consistent with the low transparency of a metal. Further calculations have shown that the background level rises in dark-field as the period Λ reduces, suggesting that improved imaging will be obtained with isolated features.

3. Experimental results

Experiments were performed on NEMS fabricated in bonded-silicon-on-insulator with a device layer thickness of 4 μm. NEMS parts were patterned by STL using gold sidewall mask with a constant width of 0.1 μm, while MEMS parts were defined by photolithography with a minimum width of 2.0 μm. Patterns were transferred into the device layer using an inductively coupled plasma etcher. Photoresist used to define microscale parts was stripped, but gold sidewall

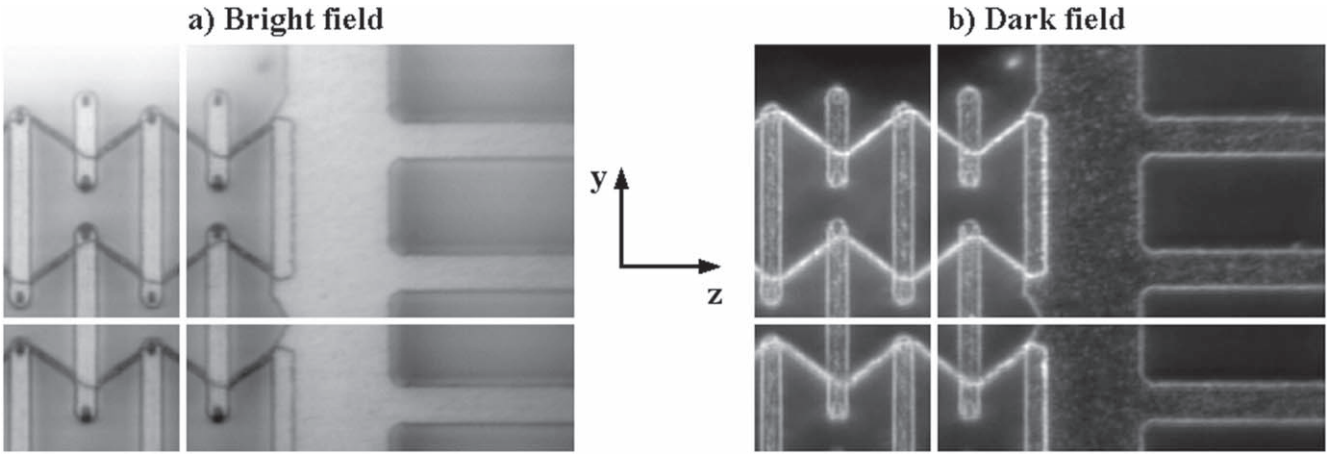

Figure 5. Optical images of an example high-aspect-ratio NEMS device, obtained with (a) bright- and (b) dark-field illumination. Lines are trajectories for detailed examination.

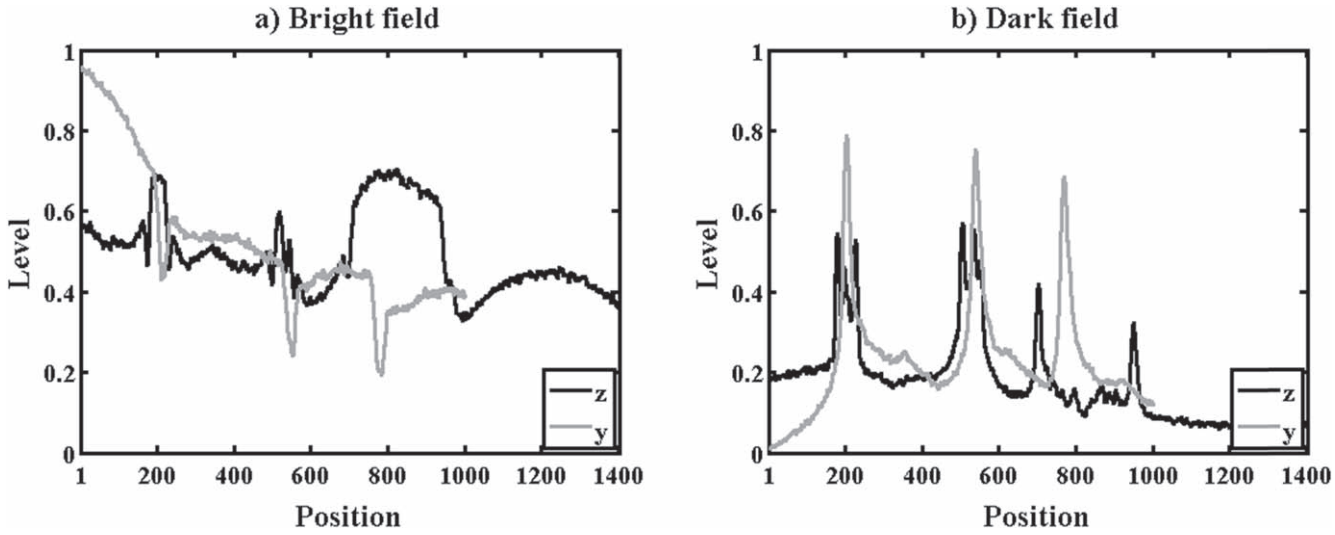

Figure 6. (a) and (b) line scans along the *y*- and *z*-trajectories in figures 5(a) and (b).

material was left in place. Devices were freed from the substrate by undercut.

Microscopy was performed using a Zeiss Axiotech equipped with Epiplan lenses that allowed bright- and dark-field illumination. The best results were obtained using a x50 objective with NA = 0.7. Images were captured in black-and-white using an AmScope MU1400B digital camera. Image processing carried out using Matlab involved (1) compensation for shifts caused by the mode selector, (2) cropping to selected regions, (3) normalization and (4) feature extraction as described below. Clean substrates were required to avoid spurious features.

Figure 5 shows optical microscope photos of an example NEMS, namely a section of cellular material formed from 0.1 μm wide flexible beams and 2 μm wide rigid bars, attached to a MEMS comb electrode. Figure 5(a) shows the structure in bright field. As predicted, nanoscale features are visible as dark lines, and microscale features by their edges. Rounded corners and small circular features are artifacts of lithography. Diffraction from the cellular structure has caused the apparent brightness of the substrate to vary, although the variation is small. However, there are larger variations in brightness elsewhere. Figure 5(b) shows the dark field image. The brightness scale has reversed, with nanostructures now appearing as bright lines and microstructure outlines less bright. The substrate is dark, and the variation outside the cellular material has reduced.

Figures 6(a) and (b) show line scans in the *y*- and *z*-directions obtained from the two images in figure 5, which have been chosen to cross nano- and microscale features, respectively. For the bright-field image, the modulation associated with structural features is similar to brightness variations in substrate regions, suggesting that segmentation algorithms based simply on brightness will fail. Reduced substrate variation and improved discrimination of substrate, microstructures and nanostructures is obtained in dark-field, in qualitative agreement with the simulations of figure 2. Despite this, we have found absolute brightness to be an insufficient criterion for feature separation.

Consistently more reliable results are obtained using valley and ridge detection [12, 13], processes that enhance discrimination of curved regions of the brightness surface $B(y, z)$.

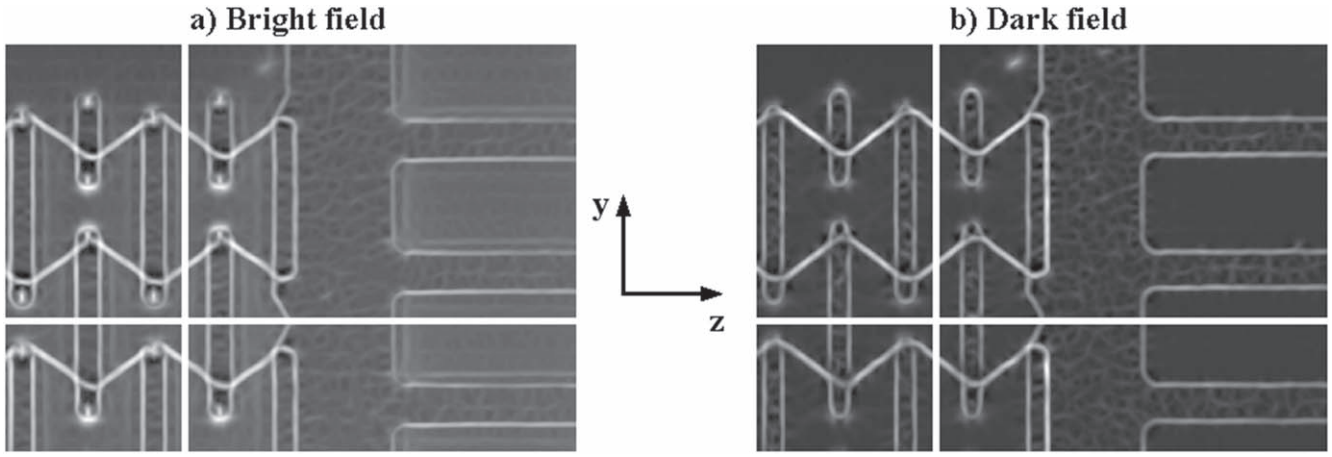

Figure 7. (a) and (b) major eigenvalue images obtained from the images in figures 5(a) and (b).

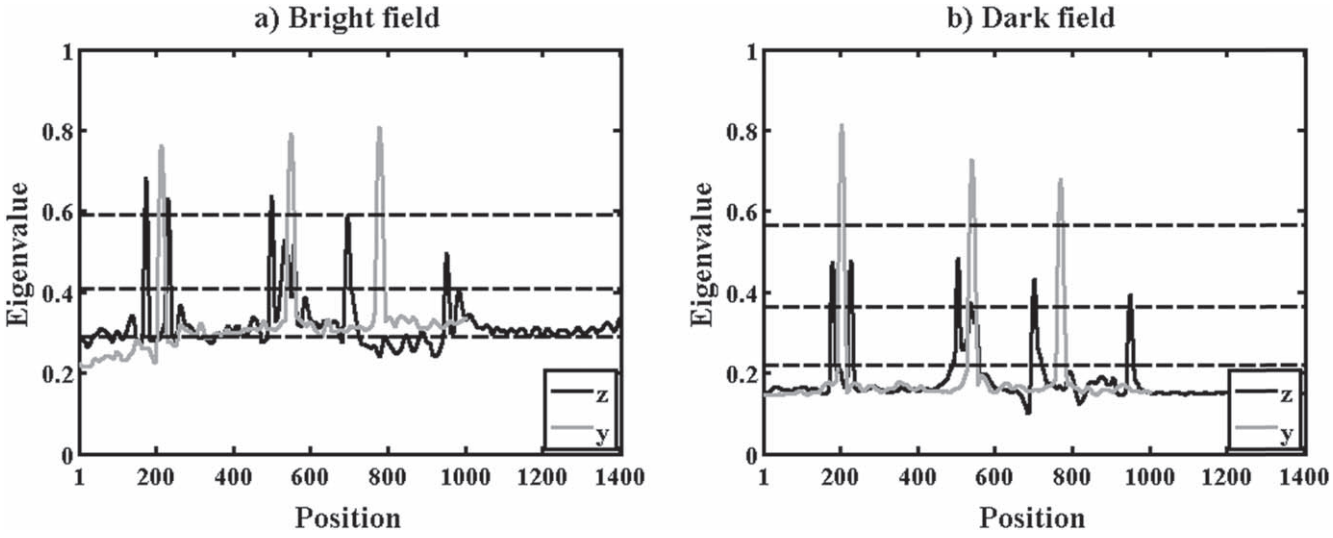

Figure 8. (a) and (b) Line-scans along the *y*- and *z*-trajectories in figures 7(a) and (b). Dashed lines are Otsu levels obtained during the image segmentation process.

The former is appropriate for bright-field images, and the latter for dark-field, but the approach is the same in each case. The brightness surface is first smoothed, by convolution with the matrix representation of a Gaussian kernel with standard deviation σ, namely $\left(\frac{1}{2\pi\sigma^2}\right)\exp\left\{-\frac{y^2+z^2}{2\sigma^2}\right\}$. The second derivatives H_{yy}, H_{zz} and H_{yz} of B are then computed by convolution of B with matrix representations of second-order differential operators. The local results are then placed in a 2×2 matrix $[H_{yy}\, H_{yz}, H_{yz}, H_{zz}]$, whose eigenvalues are found as $\lambda_{1,2} = \frac{1}{2}\{H_{yy} + H_{zz} \pm \sqrt{(H_{yy}^2 + H_{zz}^2 - 2H_{yy}H_{zz} + 4H_{yz}^2)}\}$. The eigenvalues give the principal curvatures of B, allowing valleys to be detected by identifying regions with a large positive eigenvalue. Ridges are detected similarly, as regions with a large negative eigenvalue.

Here, we refer to the significant eigenvalue in each modality as the major value, and perform all subsequent processing on its value after conversion to gray-scale. Figure 7 shows the spatial variations of the major eigenvalue of the two images in figure 5, obtained using $\sigma = 8$. The variations are similar, with nanoscale features and the edges of microscale features appearing as bright lines and exposed substrate regions being dark. However, contrast between line features and the substrate is noticeably greater in dark field. Figure 8 shows line scans in the *y*- and *z*-directions obtained from figure 7, which show how nonlinear processing has flattened the variations in substrate regions. However, the dark-field image has again yielded increased differentiation.

Feature separation is carried out using the multilevel Otsu method, which partitions a distribution into sub-groups based on threshold levels that minimize their variances [14, 15]. One obvious strategy is to segment the major eigenvalue distribution into three groups (substrate, edges of microscale features, and nanoscale features) using two levels. However, because the substrate brightness may vary, improved results are obtained using four groups (two substrate groups, microscale features and nanoscale features).

This approach requires three Otsu levels, shown as the dashed lines in figure 8. The highest level separates nanoscale features from all other groups, while the region between the highest and second highest levels separates microscale features from the substrate groups. Unfortunately, this region

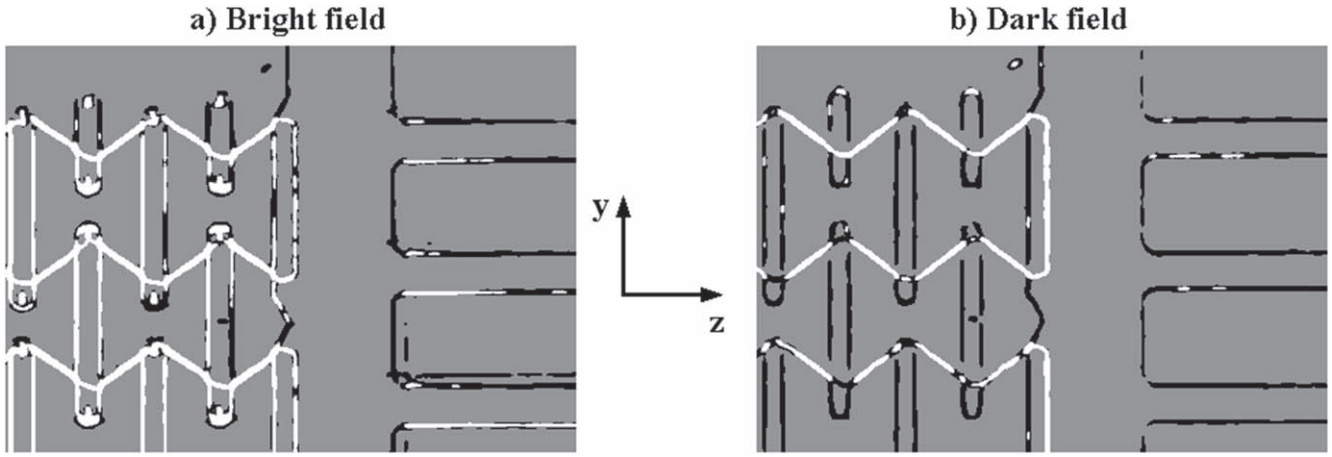

Figure 9. (a) and (b) Segmented images, obtained from figures 7(a) and (b) by valley and ridge detection, respectively, using three Otsu levels.

also contains the shoulders of nanoscale features. To suppress these regions, we have used a strategy proposed in [11]. The nanoscale pattern is extracted first, and then convolved with a small, uniform, square matrix to broaden any features therein. The resulting pattern is used as a mask to exclude the shoulders of nanoscale features during extraction of microscale features.

Figures 9(a) and (b) shows the result of applying the algorithm above to figures 7(a) and (b), respectively. Here the edges of microscale features are outlined in black and nanoscale features in white. There are clearly numerous classification errors in figure 9(a). Errors are significantly reduced in figure 9(b), which uses the dark field image as a starting point, validating earlier arguments for this modality.

Estimates of metrological performance were made as follows. Image dimensions were calibrated by comparison with mask dimensions. The actual width of 2 μm wide beams was estimated from peak locations in line-scans of image brightness eigenvalues as $2.4 \pm 0.2\,\mu$m (bright field), $2.2 \pm 0.05\,\mu$m (dark field). However, microscale feature spacing was repeatable to $\pm 0.05\,\mu$m in both cases. Dark field results therefore appear more reliable, and the explanation for line-width increase is assumed to lie in lithography. The apparent width of 100 nm wide beams was estimated from the standard deviation of Gaussian fits to similar line-scans. As expected, much larger values were obtained: 390 ± 10 nm (bright field), 360 ± 10 nm (dark field), using 100 measurements. Resolution is therefore consistent with standard microscopy, and any advantage of optical pre-processing and subsequent image processing lies in feature discrimination.

4. Conclusions

We have compared bright- and dark-field white light imaging of widely spaced, high aspect ratio nanostructures. One-dimensional models predict and experiments on silicon NEMS confirm that nanostructures will be visible in each case despite their sub-wavelength dimension, and that microstructures will be visible by their edges. Similar results are obtained for silicon and gold, with increased scattering in the latter case. Images are inverted in dark field, and largely arise from cylindrical waves scattered from edges. This modality provides increased contrast between features of interest and the substrate, leading to improved segmentation during image analysis. The advantage is inherent; due to the nature of the illumination, dark-field imaging is sensitive to scattering from the edges of raised features, but insensitive to minor variations in scattering from flat surfaces. For bright field images, increased differentiation is obtained using valley detection; here, similar advantages are obtained by ridge detection. There may be applications for the technique as a low-cost method of inspection and metrology that avoids time-consuming SEM inspection.

Acknowledgments

The authors are extremely grateful to Dr Munir Ahmad and Dr Dixi Liu for original device fabrication.

ORCID iDs

R R A Syms https://orcid.org/0000-0003-0901-8314

References

[1] Craighead H G 2002 Nanoelectromechanical systems *Science* **290** 1532–5
[2] Ekinci K L and Roukes M L 2005 Nanoelectromechanical systems *Rev. Sci. Instrum.* **76** 061101
[3] Hunter W R, Holloway T C, Chatterjee P K and Tasch A F 1981 A new edge-defined approach for submicrometer MOSFET fabrication *IEEE Electron. Dev. Lett.* **2** 4–6
[4] Hilleringmann U, Vierigge T and Horstmann J T 2000 A structure definition technique for 25 nm lines of silicon and related material *Microelectron. Eng.* **53** 569–72

[5] Choi Y-K, Zhu J, Grunes J, Bokor J and Somorjai G A 2003 Fabrication of sub-10-nm silicon nanowire arrays by size reduction lithography *J. Phys. Chem.* **107** 3340–3
[6] Bhardwaj J K and Ashraf H 1995 Advanced silicon etching using high density plasmas *Proc. SPIE* **2639** 224–33
[7] Benitez A, Esteve J and Bausells J 1995 Bulk silicon microelectromechanical devices fabricated from commercial bonded and etched-back silicon-on-insulator substrates *Sensors Actuators* A **50** 99–103
[8] Liu D and Syms R R A 2014 NEMS by sidewall transfer lithography *IEEE J. Microelectromech. Syst.* **23** 1366–73
[9] Syms R R A, Liu D and Ahmad M M 2017 Nanostructured 2D cellular materials by sidewall transfer lithography NEMS *J. Micromech. Microeng.* **27** 075003
[10] Nyyssonen D and Larrabee R D 1987 Submicrometer linewidth resolution in the optical microscope *J. Res. Natl Bur. Stand.* **92** 187–204
[11] Syms R R A, Bouchaala A, Sydoruk O and Liu D 2019 Optical imaging and image analysis for high aspect ratio NEMS *J. Micromech. Microeng.* **29** 015003
[12] Haralick R M 1983 Ridges and valleys on digital images *Comput. Vis. Graph. Image Process.* **22** 28–38
[13] Eberly D, Gardner R, Morse B, Pizer S and Scharlach C 1994 Ridges for image analysis *J. Math. Imag. Vis.* **4** 353–73
[14] Otsu N 1979 A threshold selection method from gray-level histograms *IEEE Trans. Syst. Man Cybern.* **SMC-9** 62–6
[15] Liao P S, Chen T S and Chung P C 2001 A fast algorithm for multilevel thresholding *J. Inf. Sci. Eng.* **17** 713–27
[16] Hopkins H H 1953 On the diffraction theory of optical images *Proc. R. Soc.* A **217** 408–32
[17] Nyyssonen D 1982 Theory of optical edge detection and imaging of thick layers *J. Opt. Soc. Am.* **72** 1425–36
[18] Nyyssonen D and Kirk C P 1988 Optical microscope imaging of lines patterned in thick layers with variable edge geometry: theory *J. Opt. Soc. Am.* A **5** 1270–80
[19] Sheridan J T and Sheppard C J R 1993 Coherent imaging of periodic thick fine isolated structures *J. Opt. Soc. Am.* A **10** 614–32
[20] Sheridan J T and Sheppard C J R 1994 Modelling of images of square-wave gratings and isolated edges using rigorous diffraction theory *Opt. Commun.* **105** 367–78
[21] Sheridan J T and Köurner T O 1995 Imaging periodic surface relief structures *J. Microscopy* **177** 95–107
[22] Tamir T, Wang H C and Oliner A A 1964 Wave propagation in sinusoidally stratified dielectric media *IEEE Trans. Microw. Theory Tech.* **MTT-12** 323–35
[23] Burkhardt C B 1966 Diffraction of a plane wave at a sinusoidally stratified dielectric grating *J. Opt. Soc. Am.* **56** 1502–609
[24] Chu R S and Kong J A 1977 Modal theory of spatially periodic media *IEEE Trans. Microw. Theory Tech.* **MTT-25** 18–24
[25] Moharam M G and Gaylord T K 1983 Three-dimensional vector coupled wave analysis of planar-grating diffraction *J. Opt. Soc. Am.* **73** 1105–12
[26] Moharam M G and Gaylord T K 1983 Rigorous coupled-wave analysis of grating diffraction—*E*-mode polarization and losses *J. Opt. Soc. Am.* **73** 451–5
[27] Keller J B 1962 Geometrical theory of diffraction *J. Opt. Soc. Am.* **52** 116–30
[28] Ufimtsev P Y 1971 Method of edge waves in the physical theory of diffraction *US Air Force Foreign Technology Division Translation* FTD-HC-23-259-71 Wright-Patterson AFB, OH